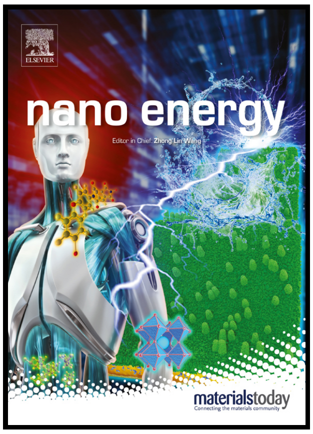

Coupling Layered Spraying with Joule Heating to Achieve Efficient CuZn Alloy Synthesis for Self-Powered Nitrate Reduction to Ammonia

Shuaitong Wang, Yang Liu, Jinrui Huang, Shizhe Liu, Shilong Li, Mengran Liu, Zhichao Ma, Tianfang Yang, Yingjie Yang, Shuyan Gao

PII: S2211-2855(25)00202-2
DOI: https://doi.org/10.1016/j.nanoen.2025.110843
Reference: NANOEN110843

To appear in: *Nano Energy*

Received date: 16 January 2025
Revised date: 15 February 2025
Accepted date: 3 March 2025

Please cite this article as: Shuaitong Wang, Yang Liu, Jinrui Huang, Shizhe Liu, Shilong Li, Mengran Liu, Zhichao Ma, Tianfang Yang, Yingjie Yang and Shuyan Gao, Coupling Layered Spraying with Joule Heating to Achieve Efficient CuZn Alloy Synthesis for Self-Powered Nitrate Reduction to Ammonia, *Nano Energy,* (2025) doi:https://doi.org/10.1016/j.nanoen.2025.110843

Coupling Layered Spraying with Joule Heating to Achieve Efficient CuZn Alloy Synthesis for Self-Powered Nitrate Reduction to Ammonia

Shuaitong Wang[a], *Yang Liu*[b], *Jinrui Huang*[b], *Shizhe Liu*[a], *Shilong Li*[a], *Mengran Liu*[b], *Zhichao Ma*[b], *Tianfang Yang*[a], *Yingjie Yang*[a], *Shuyan Gao*[ab]*

[a] School of Chemistry and Chemical Engineering, Henan Normal University, Xinxiang, Henan 453007, P. R. China

[b] School of Materials Science and Engineering, Henan Normal University, Xinxiang, Henan 453007, P. R. China

E-mail address: shuyangao@htu.edu.cn

Abstract

Electrochemical reduction of nitrate to ammonia (NO_3RR) is an emerging and environmentally sustainable approach for synthesizing ammonia (NH_3). However, the electrocatalytic NO_3RR faces significant challenges of the slow kinetics of active hydrogen (*H) transfer and extreme dependence on conventional energy sources. Herein, we innovatively propose a novel strategy of layered spraying coupled with a Joule heating strategy to prepare a $CuZn_5$ alloy for enhancing the adsorption energy of *H and reducing the desorption energy of NH_3, which is guided by density functional theory (DFT) calculations. The synthesized $CuZn_5$ alloy exhibits exceptional performance, with a remarkable NH_3 Faradaic efficiency reaching 98.4% and an impressive yield rate of 420 $\mu mol\ h^{-1}\ cm^{-2}$. Furthermore, the $CuZn_5$ catalyst is integrated into a self-powered NO_3RR

system, which is powered by a high-performance triboelectric nanogenerator (I_{max} = 100 μA, V_{max} = 600 V), achieving an NH_3 yield rate of 54.70 μmol h^{-1} cm^{-2} without the external power source. This study presents a novel method for the efficient preparation of NO_3RR catalysts and offers a clean energy solution for the production of high-value chemicals.

Keywords: Cu-Zn alloy catalyst, active hydrogen, Joule heating, triboelectric nanogenerator, self-powered NO_3RR system.

1. Introduction

Ammonia (NH_3) is a crucial industrial chemical and is considered to be an ideal zero-carbon-emission energy carrier [1,2]. The electrochemical nitrate reduction reaction (NO_3RR) not only mitigates environmental pollution but also enables the efficient recycling of nitrogen resources [3,4], offering a sustainable alternative to the conventional Haber-Bosch method [5,6]. Given that the NO_3RR involves an eight-electron coupled with a nine-proton transfer process, which is generally facilitated by active hydrogen (*H) produced from the dissociation of water [7,8]. Therefore, it is imperative to develop electrocatalysts that can regulate the adsorption strength of N-containing intermediates and *H to boost the selectivity and efficiency of the transformation from NO_3^- to NH_3 [6,9,10].

Cu is regarded as a promising high-performance catalyst for NO_3RR due to its similar energy level to NO_3^- and the highly occupied d-orbitals [11–13]. However, the weak adsorption of *H on Cu at low overpotentials constrains the hydrogenation rate, thereby limiting the yield of NH_3. While the coverage of *H increases at high overpotentials, the competitive hydrogen evolution reaction (HER) dominates the NO_3RR process, resulting in a reduction of Faradaic efficiency (FE) [14,15]. The introduction of various metals into Cu-based alloys aids in reconstructing the surface atomic structure, thus strengthening the bond between *H and the active sites [16,17]. Meanwhile, metals with low work function can effectively suppress competitive HER and enhance the adsorption of *H [18]. The work function value of Zn is 4.01 eV, which is lower than that of other metals commonly used in NO_3RR, including Cu (4.53 eV), Fe (4.31 eV), Co (4.52 eV), and Ni (4.98 eV). This results in a higher electronic activity on the material surface of Zn that facilitates the adsorption of *H [19,20]. However, the significant differences in reduction potentials and boiling points between the Cu and Zn elements render the synthesis of CuZn alloys typically involving multi-step, energy-intensive, and time-consuming processes, such as high-temperature vapor deposition [21], electrodeposition [22,23], and mechanical alloying [24]. It is therefore crucial to establish a rapid and effective technique for synthesizing CuZn alloys.

Additionally, the substitution of conventional energy sources with clean energy sources to drive NO_3RR can mitigate environmental contamination [25,26]. Recent years have seen a significant increase in the research and development of triboelectric nanogenerators (TENGs). These devices have been demonstrated to be highly effective in converting renewable energy sources into electrical energy, such as wind and wave power, through the utilization of triboelectric charging and electrostatic induction mechanisms [27]. Due to a series of advantages such as lightweight, ease of manufacturing, and strong environmental adaptability [28,29], various TENGs have been employed to facilitate the conversion of diverse renewable energy sources into electrical energy for a range of electrochemical reactions, including seawater electrolysis for hydrogen production [30,31], electrochemical nitrogen reduction [32], and organic pollutant degradation [33,34], among others. However, the low current and high voltage of TENGs are not aligned with the reaction conditions of NO_3RR, resulting in a low ammonia yield of self-powered NO_3RR. Consequently, constructing a reasonable circuit system to overcome the matching barrier between TENG and NO_3RR is important for achieving self-powered NO_3RR [35,36].

In this work, Zn with a low work function was selected as the target component for a Cu-based alloy, and a $CuZn_5$ alloy structure was designed and constructed using density functional theory (DFT) calculations. Theoretical studies indicated that the addition of Zn is more conducive to the adsorption of *H, thereby accelerating the hydrogenation process and further reducing the desorption energy of NH_3. Experimentally, a layered spraying coupled with a Joule heating strategy was employed for the preparation of $CuZn_5$ alloy catalysts. The prepared $CuZn_5$ alloy catalyst exhibited a FE of up to 98.4% and an NH_3 yield rate of 420 μmol h^{-1} cm^{-2} at −0.25 V vs. the reversible hydrogen electrode (RHE) in 0.5 M K_2SO_4 and 0.1 M KNO_3 solution. Moreover, the construction of a circuit system integrating the developed high-performance TENG (I_{max} = 100 μA, V_{max} = 600 V) with the NO_3RR system, an NH_3 yield rate of 54.70 μmol h^{-1} cm^{-2} has been attained without the necessity for an additional external power source. This study not only introduces an innovative strategy for the rapid preparation of NO_3RR catalysts, but also provides an alternative solution for creating valuable chemicals using renewable energy.

2. Experimental section

2.1. Chemicals and Materials

Copper(II) nitrate trihydrate ($Cu(NO_3)_2·3H_2O$, analytical reagent (AR)), zinc nitrate hexahydrate ($Zn(NO_3)_2·6H_2O$, assay ≥ 99%), potassium sulfate (K_2SO_4, assay ≥ 99%), potassium nitrate (KNO_3, assay ≥ 99%), sodium hypochlorite (NaClO, with an available chlorine content exceeding 5.0%), anhydrous ethanol (C_2H_6O, assay ≥ 99.7%), sodium salicylate ($C_7H_5O_3Na$, assay ≥ 99.5%), sodium hydroxide (NaOH, assay ≥ 96%), ammonium chloride (NH_4Cl, assay ≥ 99%), and sodium nitroferricyanide ($C_5FeN_6Na_2O·2H_2O$, assay ≥ 99%) were obtained from Aladdin Chemical Reagents Co., Ltd. The chemical reagents listed above were utilized without further purification or treatment. Carbon fiber paper (CFP) was procured from Suzhou Sinerno Technology Co., Ltd. For the execution of the experiment, all solutions were meticulously prepared utilizing ultrapure water, which exhibited a resistivity measurement of 18.25 MΩ. Copper foils (110 μm thick) and FEP films (50 μm thick) were sourced from DuPont, USA. PLA (1.75 μm diameter) was supplied by Esun Co., Ltd.

2.2. Catalyst Synthesis

To commence, a sequence of solutions with varying molar concentrations of $Cu(NO_3)_2·3H_2O$ and $Zn(NO_3)_2·6H_2O$ was meticulously prepared. The $Cu(NO_3)_2·3H_2O$ was standardized at a molar concentration of 0.15 M, whereas the $Zn(NO_3)_2·6H_2O$ concentrations were incrementally adjusted from 0.03 M to 0.15 M in intervals of 0.03 M. The resulting catalysts, derived from distinct solution mixtures, were denoted as Cu_xZn_y, representing the molar ratios of copper to zinc in a gradient from 1:0.2 to 1:1.0. The carbon fiber paper (1 × 10 cm) was subjected to a brief calcination process over an alcohol lamp to augment their hydrophilic attributes. Subsequently, a precisely measured 3 mL aliquot of the prepared $Zn(NO_3)_2·6H_2O$ solution was uniformly sprayed onto the pre-conditioned carbon fiber paper utilizing an aerosolization device (produced by Komax Ltd., China). The paper underwent a vacuum drying regimen at 50 °C for 6 h after the application of the spray. The aforementioned procedure was reiterated with a 3 mL aliquot of $Cu(NO_3)_2 \cdot 3H_2O$ solution, followed by a subsequent vacuum drying phase at 50 °C for 6 h. Finally, the carbon paper loaded with metal precursor was carried out to a Joule heating system (CIS-JH3.3-P, Hefei In Situ Technology Co., Ltd., China) in a H-Ar (10% H_2) atmosphere for 5 s (800 °C, 160 °C s^{-1}), and after rapid cooling, a copper-zinc alloy catalyst was obtained.

2.3. Material Characterization

Transmission electron microscopy (TEM) imaging was executed on a JEM-2100F instrument, procured from Jeol Ltd., Japan. The morphological examination of the catalyst's surface was meticulously performed employing a Zeiss SUPRA40 scanning electron microscope (SEM). Subsequent elemental mapping was ascertained through energy-dispersive X-ray spectroscopy (EDS). Analyses about the crystallographic texture and phase assemblage were undertaken using a Tiamer X-ray diffractometer, fabricated by Malvern Panalytical, in conjunction with a Cu-Kα radiation source. X-ray photoelectron spectroscopic (XPS) investigations were facilitated on a ThermoScientific ESCALAB250Xi platform, with the C 1s orbital peak at 284.8 eV harnessed for calibration of binding energies. Acquisition of crystalline structural data was effected via a PANalytical B.V. XPert3 X-ray powder diffractometer. In addition, the ultraviolet-visible absorption spectral analysis of the samples was using a LAMBDA 1050+ spectrophotometer, supplied by PerkinElmer, Inc.

2.4. Electrochemical Characterization of NO_3RR

The electrochemical tests were conducted in an H-cell equipped with a pre-cleaned Celgard 3501 separator membrane using ethanol and deionized water. The measurements were taken using a DH7000 workstation from Donghua Technologies, employing a standard three-electrode setup. A copper-zinc alloy catalyst mounted on carbon fiber paper acted as the working electrode, while a saturated calomel electrode (SCE) was used as the reference electrode, and a platinum foil of 1 cm^2 area served as the counter electrode. The electrolyte for the electrocatalytic nitrate reduction in both the cathode and anode compartments consisted of a solution containing 0.1 M KNO_3 and 0.5 M K_2SO_4. The chamber of the H-cell, each holding 30 mL of the electrolyte solution, was purged with high-purity argon to eliminate oxygen before the experiments. All experimental measurements were calibrated against the SCE reference and transformed to the reversible hydrogen electrode (RHE) potential, applying the conversion: $E_{\mathrm{RHE}} = E_{\mathrm{SCE}} + 0.95$ V. The transformation was ascertained by gauging the potential gap between the reversible hydrogen and SCE using an AVO multimeter. Linear sweep voltammetry (LSV) tests were carried out at a scanning speed of 5 mV s^{-1} without applying iR compensation. The NO_3RR performance of the Cu_xZn_y was analyzed at various potentials (−0.05, −0.15, −0.25, −0.35, and −0.45 V vs. RHE) by collecting i-t curves three times for 30 mins each, followed by the collection of the electrolyte post-testing. The durability of the Cu_xZn_y catalyst was assessed through consecutive electrochemical cycles at −0.25 V vs. RHE. The electrochemical impedance spectroscopy (EIS) technique was used to determine the solution resistance (R_s) and charge transfer impedance (R_{ct}) of the synthesized samples at 0.05 V, scanning frequencies from 0.1 Hz to 100 kHz.

By employing a UV-visible spectrophotometer and the indophenol blue method, we measured the concentration of NH_3 generated in the electrolyte after performing chronoamperometry. After the experiment, the electrolyte solution was evenly diluted to a degree of 50 times its original volume. Subsequently, 0.5 mL each of color reagent A (a mixture of 100 mL deionized water, 0.5 g of NaOH, and 1 mL NaClO) and color reagent B (a mixture of 50 mL deionized water, 5 g of $C_7H_5O_3Na$, 0.02 g of $C_5FeN_6Na_2O\cdot 2H_2O$, and 0.25 g of NaOH) were added in succession to the diluted solution.

The combined solution was allowed to rest at room temperature for 60 minutes before recording the absorbance spectrum using a UV-visible spectrophotometer, which scanned wavelengths from 550 nm to 750 nm in increments of 2 nm. The NH_3 concentration was determined by monitoring the absorbance at 660 nm, concerning a calibration curve that had been previously established.

The calculation methods for the Faradaic efficiency (FE_{NH3}) and yield rate of ammonia (Y_{NH3}) production are elaborated as follows:

$$FE_{NH_3} = 8 \times F \times C_{NH_3} \times V \,/\, Q \quad (1)$$

$$Y_{\mathrm{NH_3}} = \left(C_{\mathrm{NH_3}} \times V\right) / \left(t \times S\right) \quad (2)$$

In this study, the Faradaic constant F is 96,485.3 C mol^{-1}, wherein $C_{\mathrm{NH_3}}$ denotes the concentration of NH_3. The volume of the electrolyte V, which is 30 mL, is contained within the cathodic compartment. The total charge consumed during the reaction, expressed in coulombs (C), is represented by Q. The duration of the reaction t is 1800 s. The geometric surface area of the working electrode S, measuring 0.5 cm^2, serves as the reference for the distribution of active sites in electrochemical assays.

2.5. Structural Design and Fabrication of TENG

The layout of the TENG was designed using AutoCAD (Autodesk, Inc.) for 2D elements, and Pro/Engineer (PTC: Parametric Technology Corporation) was employed for the 3D modeling of its components. Subsequently, the finished 3D model files were uploaded into Ultimaker Cura for slicing and sent to the FDM 3D printer (Hori Z300Plus) for actual production. In this process, biodegradable polylactic acid (PLA) was selected as the printing material, and the construction of TENG components was achieved through the processes of melting, deposition, and solidification.

The TENG measures 160 mm in length, 150 mm in width, and 170 mm in height, comprising two primary components: inner rotor and outer stator, both of which are manufactured using PLA material via 3D printing technology. The inner rotor is powered by external mechanical energy via a coupling. The inner rotor is a cylinder with a height of 140 mm and a radius of 70 mm. During the design phase, the Pro/Engineer software was used to construct a petal-like structure as a support structure of the inner rotor in order to reduce its mass as well as increase its robustness. The stator consists of two symmetrical structures of 80 mm (length) × 150 mm (width) × 170 mm (height). Eight FEP films with dimensions of 140 mm × 75 mm × 110 μm are precisely placed in the grooves of the inner rotor as the loss-of-electrons part of the friction layer. In addition, two copper foils with 600 mm × 80 mm × 110 μm were used as the electron-acquiring part of the friction layer to achieve electron transfer with the FEP.

2.6. Self-Powered Electrocatalytic NO_3RR System

The performance evaluation of TENG was carried out emulating by an external driving force, utilizing an electric motor (Oriental Motor, China) to supply the necessary power. At rotational speeds between 300 and 600 rpm, an electrometer (model 6514, Keithley, USA) was employed for precise electrical charge and current measurements, with data visualization and archiving managed through LabVIEW software. Given the potential for the high voltages generated by TENGs to exceed the measurement capabilities of the electrometer, a digital oscilloscope (model DSO-X-2014A, Keysight, USA) was engaged to capture and document voltage signals that exceed the scale. This testing regimen is designed to thoroughly assess the energy conversion efficiency and electrical output characteristics of TENGs under simulated external driving forces.

This self-powered system was constituted of three core components: TENG, a control circuit, and a nitrate reduction electrolytic cell. The fabrication processes and performance evaluations of the TENG and the nitrate reduction catalyst have been elaborated in previous sections. The key components of the control circuit include a transformer (YHDC, PE2006, China), a rectifier (ASEMI, DB107, China), and a capacitor (ChongX, 3300 μF, China). By paralleling multiple transformers to match the internal resistance of the TENG, the system is capable of optimizing its output power and adapting voltage and current to align with the demands of the electrochemical setup, while the capacitor stores electrical energy and stabilizes the voltage. This design aims to optimize energy conversion efficiency, ensuring that the system can continuously and efficiently perform NO_3RR without the need for an external power source.

3. Results and discussion

3.1. Mechanistic Investigation of NO_3RR

Previous reports have indicated that metals with low work functions exhibit a lower HER activity. Firstly, we screened a series of metals commonly used in the NO_3RR based on the work function principle [18,20]. As shown in Figure 1a, Zn possesses the lowest work function (4.01 eV) compared with other metals commonly used in NO_3RR [37], suggesting its efficacy in inhibiting the HER while facilitating increased *H availability for NO_3RR.

To verify the reaction mechanism of Zn combined with Cu in NO_3RR, the $CuZn_5$ alloy was designed and constructed, followed by the performance of DFT calculations (Figure 1b). The $CuZn_5$ reaction model was constructed to describe the NO_3RR process: $^*NO_3 \rightarrow {}^*NO_2 \rightarrow {}^*NO \rightarrow {}^*N \rightarrow {}^*NH \rightarrow {}^*NH_2 \rightarrow {}^*NH_3 \rightarrow NH_3$. The results showed that the rate-determining step (RDS) involving both Cu and Zn was the desorption of $^*NH_3$, with energy barriers of 0.39 eV and 0.58 eV, respectively. However, the $CuZn_5$ alloy modulated the adsorption of intermediates, shifting the RDS to the transformation of $^*NO_2$ to *NO and reducing the energy barrier to 0.29 eV. Moreover, the $CuZn_5$ alloy notably lowered the desorption energy barrier for $^*NH_3$ to 0.13 eV, effectively promoting ammonia yield. Introducing Zn leads to the optimization of the d-band center position of Cu, ensuring appropriate adsorption of reaction intermediates and accelerating the desorption process of $^*NH_3$ (Figure 1c). Further analysis of the competitive reaction as Figure 1d indicates that Cu has a high ΔG_{*H}, making it prone to HER. The $CuZn_5$ alloy exhibits a notable ΔG_{*H} of 0.36 eV, enhancing the adsorption capacity for *H and effectively inhibiting the occurrence of HER, consistent with the results from the work function principle screening. Furthermore, Figure S1 shows that the $CuZn_5$ alloy more favorably facilitates the dissociation of water.

In the $CuZn_5$ alloy, Cu sites are beneficial for the adsorption of N-containing intermediates, while Zn sites provide more *H for the reaction, thereby accelerating the hydrogenation step (Figure 1e). This discovery not only reveals the excellent performance of the $CuZn_5$ alloy catalyst but also offers a theoretical foundation for the development of new, highly efficient NO_3RR catalysts.

3.2. Catalyst Synthesis and Characterization

Based on the theoretical calculation results, the process of synthesizing the CuZn alloy catalysts (CuZn-S) by the layered spraying coupled with the Joule heating method is shown in Figure 2a. The $Zn(NO_3)_2 \cdot 6H_2O$ solution was first uniformly sprayed onto a carbon fiber substrate. Subsequently, a $Cu(NO_3)_2 \cdot 3H_2O$ solution was applied using the identical spraying method. The substrate undergoes a rapid thermal treatment at 800 °C for 5 s within an H-Ar (10% H_2) mixed gas atmosphere in a Joule heating device. This process is essential for synthesizing of the CuZn alloy catalyst. In comparison to the traditional method of dissolving the two metal salts together (Figure 2b), this method is essential for the formation of the CuZn alloy catalysts because it reduces the volatilization of Zn at high temperatures. As illustrated in Figure 2c and 2d, the layered spraying method contrasts with the conventional method of pre-mixing metal salt solutions (CuZn-X) by more effectively facilitating the coverage of $Zn(NO_3)_2 \cdot 6H_2O$ by $Cu(NO_3)_2 \cdot 3H_2O$. The mass loss of Zn metal due to evaporation was effectively reduced.

The scanning electron microscopy (SEM) and transmission electron microscopy (TEM) images of CuZn-S (Figures 2e and 2f) reveal spherical nanostructures with an average particle size of approximately 311 nm (Figure S2). The size distribution analysis exhibits that the majority of particles fall within the range of 200-500 nm, indicating a relatively uniform dispersion of the nanospheres. This can be attributed to the rapid quenching during the Joule heating process, which effectively prevents further growth of the alloy feature size during annealing. High-resolution transmission electron microscopy (HRTEM) photographs (Figure 2g and S3) additionally verify the lattice fringe distances of 0.233 nm and 0.240 nm, aligning with the lattice fringes of the $CuZn_5$ alloy, thereby confirming the formation of the $CuZn_5$ alloy in the CuZn-S sample [38]. The energy dispersive spectroscopy (EDS) elemental mapping depicted in Figure 2h for the CuZn-S sample illustrates the even spatial distribution of Cu and Zn, thereby verifying the uniformity of the composite material. In contrast, the EDS mapping image of the CuZn-X sample shown in Figure S4 indicates a significant decrease in the Zn content, proving that the layered spraying method can efficiently minimize the loss of Zn during the Joule heating process.

To facilitate a more in-depth investigation of the crystal structure and elemental composition of the samples obtained by the two synthesis methods, X-ray diffraction (XRD) and X-ray photoelectron spectroscopy (XPS) techniques were employed for detailed characterization. The XRD pattern of the CuZn-X sample displays two sharp peaks at 43.29° and 50.43°, corresponding to the (111) and (200) crystal faces of the Cu face centered cubic structure (PDF # 04-0836). The small peak at 43.2° in CuZn-X corresponds to the (100) plane of graphitic carbon (PDF # 41-1487). In contrast, the diffraction peaks at 42.193° and 43.362° of the CuZn-S sample are well indexed to (110) and (111) planes of $CuZn_5$ (PDF # 35-1152) (Figure 2i). Compared with the standard card of metallic Zn (PDF # 97-7153), neither CuZn-X nor CuZn-S shows characteristic peaks of metallic Zn.

Figure 2j shows the XPS spectra of Cu 2p, Zn 2p and C 1s, confirming the presence of Cu, Zn, and C elements in CuZn-S. Figure 2k and 2l display the XPS spectra corresponding to Cu and Zn, respectively. The Cu 2p spectrum of Cu contains Cu $2p_{3/2}$ at 932.7 eV and Cu $2p_{1/2}$ at 952.5 eV. It is noteworthy that the Cu 2p peaks of CuZn-S and CuZn-X shifted to a lower binding energy in comparison with those of the pristine Cu (Figure 2k) [23,39]. The chemical states of Cu species are systematically probed by Cu LMM Auger electron spectroscopy (AES) as shown in Figure S5. It is reveals that Cu predominantly exists in the metallic state (Cu^0) within Cu, CuZn-X, and CuZn-S, along with minor quantities of Cu^+ and Cu^{2+} species [40]. These oxidized states may be attributed to surface oxidation processes occurring during sample storage. Conversely, the Zn 2p peaks of CuZn-S and CuZn-X exhibited a shift towards higher binding energy with an increase in Zn content (Figure 2l), The binding energy of Zn $2p_{3/2}$ in CuZn-S (1044.9 eV) is slightly higher than that in CuZn-X (1044.4 eV). This is due to the electron transfer from Zn atoms to Cu atoms in the CuZn alloy, resulting in a decrease in the electron density of the Zn atoms. As the Zn content increases, the Zn 2p peak of CuZn-S shifts to higher binding energy. Thereby confirming the electron transfer between Cu and Zn and demonstrating that Zn content in CuZn-S is higher than that in CuZn-X. The binding energies at approximately 932.7 eV and 1021.7 eV indicate the existence of Cu^0 and Zn^0 in both CuZn-S and CuZn-X samples [38].

3.3. Electrocatalytic NO_3RR Performance

The electrochemical performance of the synthesized samples for NO_3RR was evaluated in a conventional three-electrode H-cell under normal conditions, utilizing an electrolyte solution of 0.5 M K_2SO_4 and 0.1 M KNO_3. The linear sweep voltammetry (LSV) curves indicate that the current density of the CuZn alloy markedly surpasses that of both Cu and Zn within the potential window of −0.4 to 0.4 V relative to the reversible hydrogen electrode (RHE), as shown in Figure 3a and S7. Notably, the $Cu_1Zn_{0.4}$ catalyst possesses higher current densities than other CuZn alloy catalysts, indicating that the $Cu_1Zn_{0.4}$ catalyst provides the most favorable NO_3RR kinetics process. Additionally, as depicted in Figure 3b, which compares the LSV curves in 0.5 M K_2SO_4 with and without the addition of 0.1 M KNO_3, the current densities for the $Cu_1Zn_{0.4}$ alloy are significantly increased across the entire potential range from −0.4 to 0.4 V versus RHE when nitrate is present, thereby validating its enhanced NO_3RR catalytic activity.

Moreover, the $Cu_1Zn_{0.4}$ catalyst exhibits a lower Tafel slope of 128.2 mV dec^{-1} compared to $Cu_1Zn_{0.2}$ (192.1 mV dec^{-1}), $Cu_1Zn_{0.6}$ (162.9 mV dec^{-1}), Cu (368.1 mV dec^{-1}), and Zn (416.4 mV dec^{-1}) in Figure 3c, indicating its superior electron transfer efficiency and quicker reaction kinetics. Furthermore, the electrochemical impedance spectroscopy (EIS) was employed to evaluate the kinetics of interfacial electron transfer. The charge transfer resistance (R_{ct}) is indicative of the electrocatalytic kinetics, with smaller values signifying more rapid reaction rates. The $Cu_1Zn_{0.4}$ exhibits the smallest semicircle diameter

(≈15.2 Ω) in the EIS plot Figure 3d, suggesting the lowest charge transfer resistance and the swiftest reaction kinetics, which is consistent with the observed Tafel slope.

Figure 3e and 3f illustrate that within the potential range from −0.05 to −0.35 V vs. RHE, the NH_3 yield rate from the $Cu_1Zn_{0.4}$ catalyst gradually ascends with the reduction of the applied potential, peaking at 420 μmol h^{-1} cm^{-2} at −0.25 V vs. RHE. Moreover, the Faradaic efficiency (FE) of the $Cu_1Zn_{0.4}$ catalyst exhibits a volcano trend, reaching a peak of 98% at −0.25 V vs. RHE. According to the standard curve of the absorbance against NH_4^+ concentration, the generated NH_3 in the electrolyte is quantified (Figure S6b). Moreover, the $Cu_1Zn_{0.4}$ catalyst demonstrates competitive FE and NH_3 yield rates in the NO_3RR electrocatalysts compared to other electrocatalysts reported in the literature (Figure S16 and Table S1) [17,41–52]. The stability of the $Cu_1Zn_{0.4}$ catalyst was observed over ten consecutive cycles at an operational potential of −0.25 V vs. RHE (Figure 3g and S8), with the NH_3 yield rates and FE remained almost constant, demonstrating the excellent cyclic stability of the $Cu_1Zn_{0.4}$ catalyst. To investigate the capacity of the $Cu_1Zn_{0.4}$ catalyst to activate H_2O to generate *H, tert-butanol (TBA) was added as a scavenger to quench *H. The LSV curves for $Cu_1Zn_{0.4}$ in the presence of TBA showed a marked decrease in current density (as seen in Figure S9), signifying the essential role of *H in the NO_3RR process.

3.4. Structural Design and Performances of 3DP-TENG

Figure 4a and S10 depict the architecture of the 3D-printed triboelectric nanogenerator (3DP-TENG), which consists of an inner rotor and two symmetrically disposed outer stators, all fabricated from polylactic acid (PLA). The inner rotor is designed with grooves to accommodate a fluorinated ethylene propylene (FEP) layer, which is an essential component of the TENG assembly. The FEP layer provides mechanical stability and electrical insulation, enhancing the overall functionality and durability of the device. In accordance with the operational mechanics of a relative-sliding TENG, the outer stators are each equipped with two pairs of complementary copper electrodes. As detailed in Figure S11, the distinctive configuration of these electrodes is engineered to streamline the assembly of the TENG. The relative motion between the rotor and stators facilitates the transfer of free electrons across the triboelectric layers, thereby generating alternating current electricity through the principle of electrostatic induction, with the mechanism detailed as follows.

Figure S12 delineates the operational states of the 3DP-TENG that are pivotal to the energy conversion cycle, highlighting the interfacial charge dynamics between the FEP film and copper foils. At the interface, a difference in electron affinity prompts a charge redistribution, causing the copper foils to accumulate positive charges and the FEP film to acquire a corresponding negative charge, as illustrated in Figure S12 (I). When the FEP film approaches the Cu-2 region, as shown in Figure S12 (II), its negative charge prompts the transfer of positive charges from the Cu-1 region to the Cu-2 region via an external circuit, which counteracts the electric field created by the negative charge on the FEP film. This charge transfer is due to the varying electronegativity of the materials. Once the FEP film makes complete contact with the Cu-2 region, the positive charges from the Cu-1 region are entirely transferred to the Cu-2 region (Figure S12 (III)). Subsequently, as the FEP film withdraws from the Cu-2 area, the positive charges on Cu-2 start to move back to the Cu-1 area, which results in a reverse flow of current in the external circuit, as depicted in Figure S12 (IV). The complete detachment of the FEP film from the Cu-2 area is indicative of the conclusion of a single charge transfer cycle. This mechanism explains the energy conversion process of the 3DP-TENG and highlights the importance of interfacial charge transfer in the functioning of TENGs.

To optimize the key performance indicators of the 3DP-TENG, including the transferred charge, current, and voltage, several innovative design strategies have been employed [32]. It can be observed that the transferred charge, current, and voltage of the 3DP-TENG increase in proportion to the rotational velocity. As illustrated in Figure 4b-d, augmenting the rotational speed from 300 to 600 rpm elicits a peak current of 100 μA, a peak voltage of 600 V, and a peak transferred charge of 0.55 μC. The amplified visualizations of the transferred charge, current, and voltage (Figure S13) highlight the output stability of the 3DP-TENG, which is crucial for maintaining a consistent power supply to downstream electrocatalytic systems.

Beyond stability, the high-voltage and low-current output traits of the 3DP-TENG pose a considerable challenge to its use in electrochemical applications. Consequently, there is an imperative requirement to alter the output characteristics of 3DP-TENG to align with the requirements of electrochemical systems. Existing research indicates that the performance of 3DP-TENG is optimized when the internal resistance of 3DP-TENG is commensurate with the external load resistance [35,36]. As illustrated in Figure 4e-g, to match the internal resistance of the 3DP-TENG to achieve maximum power output. The output power of 3DP-TENG reaches the peak when the external resistance is 10^7 Ω. The introduction of the transformer realizes both the matching of the internal resistance of 3DP-TENG and the regulation of the voltage. The series connection of 11 transformers accomplishes a well-matched internal resistance of the 3DP-TENG for optimal output power, as shown in the transformer series connection diagram in Figure 4h. Concurrently, the serial connection of transformers effectively reduces the output voltage of 3DP-TENG while enhancing the output current, providing an ideal solution for 3DP-TENG to serve as a power supply device for electrochemical systems (Figure 4i).

3.5. Self-powered Electrocatalytic NO_3RR System

Figure 5a illustrates the schematic of the self-powered NO_3RR system consisting of three essential components: the 3DP-TENG acts as a standalone energy harvester, supplying power to the electrochemical device, with a control circuit that adapts the electrical output from the 3DP-TENG to fit the specific demands of the electrocatalytic system, and an electrocatalytic nitrate reduction cell that realizes the transfer of electrical energy into chemical energy. The electrical output of the 3DP-TENG undergoes rectification to direct current following attenuation and amplification via a cascade of transformers, ensuring optimal voltage levels for subsequent energy storage. Then, the current is then efficiently captured in capacitors, which serve to stabilize the fluctuations of voltage and current fluctuations. The electrical energy accumulated in these capacitors is subsequently harnessed to directly power the electrochemical cell, promoting the NO_3RR process.

As depicted in Figure 5b, the discharge efficiency of the 3DP-TENG is characterized by the rate of capacitor charging. Notably, a 3.3 mF capacitor is efficiently charged to a voltage of 2.5 V within 30 s, demonstrating the high charging efficacy of the system. In contrast, a larger capacitance of 13.2 mF reaches a charging voltage of 1.0 V under identical conditions, underscoring the inverse relationship between capacitance and voltage rise rate, which is a critical parameter in the context of energy storage and discharge in self-powered electrochemical systems.

Furthermore, the charging efficiency of the capacitors is quantified through the formula $W = 0.5 \times CU^2$, the energy stored in the capacitor is denoted as W, the capacitance is denoted C, and U is the voltage across the capacitor during the charging process. As evidenced in Figure S14a, capacitors with smaller capacitance values generally exhibit higher charging efficiencies. The operational voltage range for the NO_3RR has been determined to be 2.8 V, derived from the potential at which the $Cu_1Zn_{0.4}$ catalyst demonstrates the onset of competitive HER when supplied by an external direct current power source.

Figure 5c and S14b depict the charging dynamics of capacitors with diverse capacitances up to a threshold voltage of 2.8 V, and a meticulous analysis was conducted on their subsequent discharge characteristics. Capacitors with larger capacitance values are capable of retaining a more substantial charge, thereby sustaining an output current of approximately 22 mA over an extended duration, which is essential for maintaining consistent and stable power delivery to the electrocatalytic system. Nevertheless, these higher capacitance capacitors require a longer period to achieve the optimal operating potential necessary for the NO_3RR. To elucidate the balance between charging efficiency and discharge current, the system was subjected to a one-hour operational test at a TENG rotation speed of 500 rpm, utilizing capacitors with capacitances of 3.3 mF, 6.6 mF, 9.9 mF, and 13.2 mF to energize the NO_3RR system. As illustrated in Figure 5d, e, and S15, the maximized NH_3 yield rate is achieved at 54.70 μmol h^{-1} cm^{-2} under conditions where the capacitance is precisely calibrated to 6.6 mF.

4. Conclusions

In this work, we selected Zn with a low work function as the target component for a Cu-based alloy and designed the $CuZn_5$ alloy structure using DFT calculations. A layered spraying coupled with Joule heating strategy was employed to prepare the $CuZn_5$ alloy catalyst, achieving an exceptional NH_3 FE of 98.4% and a considerable yield rate of 420 μmol h^{-1} cm^{-2} at −0.25 V. This strategy not only facilitated the expeditious synthesis of the alloy catalyst but also mitigated the volatilization of the target component Zn under high temperatures. Furthermore, the high-performance TENG was integrated with the NO_3RR system to form a self-powered NO_3RR system, achieving an NH_3 yield rate of 54.70 μmol h^{-1} cm^{-2} without the need for an external power source, offering a novel approach to the generation of high-value chemicals driven by clean energy. Self-powered ammonia production holds significant potential for industrial application due to its ability to reduce reliance on fossil fuels and lower carbon emissions. Key opportunities include advancements in efficient catalysts, integration with renewable energy sources, and modular design for decentralized production. However, some challenges still exist, such as the output characteristics of TENGs, which are characterized by low current and high voltage, posing a mismatch issue for electrochemical systems. Additionally, the durability of TENGs and catalysts still needs to be enhanced, as well as addressing the issue of energy storage after conversion. Overall, self-powered ammonia synthesis is a promising green energy conversion technology.

Acknowledgments

This work was supported by the National Natural Science Foundation of China (Grant No. U22A20253). The DFT calculations were performed on Tianhe-2 at the Shanxi Supercomputing Centre of China.

Appendix A. Supplementary data

Supplementary material related to this article can be found in the online version, at doi:

References

[1] J. John, D. R. MacFarlane, A. N. Simonov, The why and how of NOx electroreduction to ammonia, Nat. Catal. 6 (2023) 1125–1130. https://doi.org/10.1038/s41929-023-01060-w.

[2] G.-F. Chen, Y. Yuan, H. Jiang, S.-Y. Ren, L.-X. Ding, L. Ma, T. Wu, J. Lu, H. Wang, Electrochemical reduction of nitrate to ammonia via direct eight-electron transfer using a copper–molecular solid catalyst, Nat. Energy 5 (2020) 605–613. https://doi.org/10.1038/s41560-020-0654-1.

[3] Y. Liu, J. Ma, S. Huang, S. Niu, S. Gao, $Ni_{0.25}Cu_{0.5}Sn_{0.25}$ nanometallic glasses as highly efficient catalyst for electrochemical nitrate reduction to ammonia, Nano Energy 117 (2023) 108840. https://doi.org/10.1016/j.nanoen.2023.108840.

[4] Z. Zhang, Y. Liu, X. Su, Z. Zhao, Z. Mo, C. Wang, Y. Zhao, Y. Chen, S. Gao, Electro-triggered Joule heating method to synthesize single-phase CuNi nano-alloy catalyst for efficient electrocatalytic nitrate reduction toward ammonia, Nano Res. 16 (2023) 6632–6641. https://doi.org/10.1007/s12274-023-5402-y.

[5] Z. Jiang, Y. Wang, Z. Lin, Y. Yuan, X. Zhang, Y. Tang, H. Wang, H. Li, C. Jin, Y. Liang, Molecular electrocatalysts for rapid and selective reduction of nitrogenous waste to ammonia, Energy Environ. Sci. 16 (2023) 2239–2246. https://doi.org/10.1039/D2EE03502B.

[6] L. Wu, J. Feng, L. Zhang, S. Jia, X. Song, Q. Zhu, X. Kang, X. Xing, X. Sun, B. Han, Boosting electrocatalytic nitrate-to-ammonia via tuning of nintermediate adsorption on a zn cu catalyst, Angew. Chem. Int. Ed. 62 (2023) e202307952. https://doi.org/10.1002/anie.202307952.

[7] Y. Yu, Y. Li, Y. Fang, L. Wen, B. Tu, Y. Huang, Recent advances of ammonia synthesis under ambient conditions over metal-organic framework based electrocatalysts, Appl. Catal. B 340 (2024) 123161. https://doi.org/10.1016/j.apcatb.2023.123161.

[8] S. Liang, X. Teng, H. Xu, L. Chen, J. Shi, H* species regulation by Mn-Co$(OH)_2$ for efficient nitrate electroreduction in neutral solution, Angew. Chem. Int. Ed. 136 (2024), e202400206. https://doi.org/10.1002/anie.202400206.

[9] Y. Zhao, Y. Liu, Z. Zhang, Z. Mo, C. Wang, S. Gao, Flower-like open-structured polycrystalline copper with synergistic multi-crystal plane for efficient electrocatalytic reduction of nitrate to ammonia, Nano Energy 97 (2022) 107124. https://doi.org/10.1016/j.nanoen.2022.107124.

[10] Y. Zhou, L. Zhang, Z. Zhu, M. Wang, N. Li, T. Qian, C. Yan, J. Lu, Optimizing intermediate adsorption over PdM (M=Fe, Co, Ni, Cu) bimetallene for boosted nitrate electroreduction to ammonia, Angew. Chem. Int. Ed. 63 (2024) e202319029. https://doi.org/10.1002/anie.202319029.

[11] Y. Wang, W. Zhou, R. Jia, Y. Yu, B. Zhang, Unveiling the activity origin of a Copper-based electrocatalyst for selective nitrate reduction to ammonia, Angew. Chem. Int. Ed. 132 (2020) 5388–5392. https://doi.org/10.1002/anie.201915992.

[12] L. Bai, F. Franco, J. Timoshenko, C. Rettenmaier, F. Scholten, H. S. Jeon, A. Yoon, M. Rüscher, A. Herzog, F. T. Haase, S. Kühl, S. W. Chee, A. Bergmann, R. C. Beatriz, Electrocatalytic nitrate and nitrite reduction toward ammonia using Cu_2O nanocubes: active species and reaction mechanisms, J. Am. Chem. Soc. 46 (2024) 9665–9678. https://doi.org/10.1021/jacs.3c13288.

[13] Y. Liu, S. Huang, J. Lu, S. Niu, P. K. Shen, Z. Hu, P. Tsiakaras, S. Gao, $Ni_{0.25}Cu_{0.5}Sn_{0.25}$ nanometallic glasses as highly efficient catalyst for electrochemical nitrate reduction to ammonia, Adv. Funct. Mater. 34 (2024) 2411325. https://doi.org/10.1002/adfm.202411325.

[14] Y. Bu, C. Wang, W. Zhang, X. Yang, J. Ding, G. Gao, Electrical pulse-driven periodic self-repair of Cu-Ni tandem catalyst for efficient ammonia synthesis from nitrate, Angew. Chem. Int. Ed. 62 (2023) e202217337. https://doi.org/10.1002/anie.202217337.

[15] P. Li, R. Li, Y. Liu, M. Xie, Z. Jin, G. Yu, Pulsed nitrate-to-ammonia electroreduction facilitated by tandem catalysis of nitrite intermediates, J. Am. Chem. Soc. 145 (2023) 6471–6479. https://doi.org/10.1021/jacs.3c00334.

[16] X. Wang, P. Ouo, J. Wickso, Y. Xie, Y. Wang, J. Li, J. Tam, D. Reno, J. Y. Howe, Z. Wang, A. Ozden, Y. Z. Finfrock, Y. Xu, Y. Li, A. S. Rasouli, K. Bertens, A. H. lp, M. Graetzelo, D Sinton, E. H. Sargento, Gold-in-copper at low *CO coverage enables efficient electromethanation of CO_2, Nat. Commun. 12 (2021) 3387. https://doi.org/10.1038/s41467-021-23699-4.

[17] Y. Zhang, X. Chen, W. Wang, L. Yin, J. C. Crittenden, Electrocatalytic nitrate reduction to ammonia on defective Au_1Cu (111) single-atom alloys, Appl. Catal. B 310 (2022) 121346. https://doi.org/10.1016/j.apcatb.2024.124294.

[18] O. Q. Carvalho, R. Marks, H. K. K. Nguyen, M. E. Vitale-Sullivan, S. C. Martinez, L. Árnadóttir, K. A. Stoerzinger, Role of electronic structure on nitrate reduction to ammonium: a periodic journey, J. Am. Chem. Soc. 144 (2022) 14809–14818. https://doi.org/10.1021/jacs.2c05673.

[19] Z.-H. Xue, H.-C. Shen, P. Chen, G.-X. Pan, W.-W. Zhang, W.-M. Zhang, S.-N. Zhang, X.-H. Li, C. T. Yavuz, Boronization of nickel foam for sustainable electrochemical reduction of nitrate to ammonia, ACS Energy Lett. 8 (2023) 3843–3851. https://doi.org/10.1021/acsenergylett.3c01139.

[20] J. Li, J. Hu, M. Zhang, W. Gou, S. Zhang, Z. Chen, Y. Qu, Y. Ma, A fundamental viewpoint on the hydrogen spillover phenomenon of electrocatalytic hydrogen evolution, Nat. Commun. 12 (2021) 3502. https://doi.org/10.1038/s41467-021-23750-4.

[21] Ge Yin, H. Abe, R. Kodiyath, S. Ueda, N. Srinivasan, A. Yamaguchi, M. Miyauchi, Selective electro- or photo-reduction of carbon dioxide to formic acid using a Cu–Zn alloy catalyst, J. Mater. Chem. A 5 (2017) 12113–12119. https://doi.org/10.1039/C7TA00353F.

[22] Y. Zhang, B. Xu, B. Huang, T. He, F. Meng, W. Tian, Y. Zhu, J. Wu, H. Wang, H. Li, J. Chen, Color-neutral smart window enabled by gradient reversible alloy deposition, ACS Energy Lett. 9 (2024) 4162–4171. https://doi.org/10.1021/acsenergylett.4c01677.

[23] Z. Zhang, S. Li, Y. Rao, L. Yang, W. Yan, Hao. Xu, Three-dimension porous Zn-Cu alloy: An inexpensive electrocatalyst for highly selective CO_2 reduction to CO in non-

aqueous electrolyte, Chem. Eng. J. 479 (2024) 147376. https://doi.org/10.1016/j.cej.2023.147376.

[24] A. Herzog, M. Rüscher, H. S. Jeon, J. Timoshenko, C. Rettenmaier, U. Hejral, E. M. Davis, F. T. Haase, D. Kordus, S. Kühl, W. Frandsen, A. Bergmann, B. Roldan Cuenya, Time-resolved operando insights into the tunable selectivity of Cu–Zn nanocubes during pulsed CO_2 electroreduction, Energy Environ. Sci. 479 (2024) 147376. https://doi.org/10.1039/d4ee02308k.

[25] C. Men, X. Liu, Y. Chen, S. Liu, S. Wang, S. Gao, Cotton-assisted dual rotor-stator triboelectric nanogenerator for real-time monitoring of crop growth environment, Nano Energy 101 (2022) 107578. https://doi.org/10.1016/j.nanoen.2022.107578.

[26] S. Liu, Y. Liu, Y. Chen, S. Wang, C. Men, S. Gao, Novel 3D printed vortex-like flexible roller-compacted triboelectric nanogenerator for self-powered electrochemical degradation of organic contaminants, ACS Appl. Mater. Interfaces 14 (2022) 17426–17433. https://doi.org/10.1021/acsami.2c01750.

[27] P. Wu, P. Yang, Z. Liu, G. Huang, X. Tao, S. Qin, X. Dong, L. Zheng, H. Li, X. Chen, Z. L. Wang, Boosting the output of liquid–solid triboelectric nanogenerator by an external charge-pumping strategy, Adv. Energy Mater. 14 (2024) 2303912. https://doi.org/10.1002/aenm.202303912.

[28] J. Han, Y. Feng, P. Chen, X. Liang, H. Pang, T. Jiang, Z. L. Wang, Wind-driven soft-contact rotary triboelectric nanogenerator based on rabbit fur with high performance and durability for smart farming, Adv. Funct. Mater. 32 (2022) 2108580. https://doi.org/10.1002/adfm.202108580.

[29] J. Han, Y. Liu, Y. Feng, T. Jiang, Z. L. Wang, Achieving a large driving force on triboelectric nanogenerator by wave-driven linkage mechanism for harvesting blue energy toward marine environment monitoring, Adv. Energy Mater. 13 (2023) 2203219. https://doi.org/10.1002/aenm.202203219.

[30] B. Zhang, C. Zhang, O. Yang, W. Yuan, Y. Liu, L. He, Y. Hu, Z. Zhao, L. Zhou, J. Wang, Z. L. Wang, Self-powered seawater electrolysis based on a triboelectric nanogenerator for hydrogen production, ACS Nano 16 (2022) 15286–15296. https://doi.org/10.1021/acsnano.2c06701.

[31] Y. Feng, J. Han, M. Xu, X. Liang, T. Jiang, H. Li, Z. L. Wang, Blue energy for green hydrogen fuel: a self-powered electrochemical conversion system driven by triboelectric nanogenerators, Adv. Energy Mater. 12 (2022) 2103143. https://doi.org/10.1002/aenm.202103143.

[32] S. Gao, Y. Zhu, Y. Chen, M. Tian, Y. Yang, T. Jiang, S. Gao, Z. L. Wang, Self-power electroreduction of N_2 into NH_3 by 3D printed triboelectric nanogenerators, Mater. Today 28 (2019) 17–24. https://doi.org/10.1016/j.mattod.2019.05.004.

[33] M. Tian, Y. Zhu, Y. Chen, X. Liu, Y. Yang, S. Gao, Template-assisted self-activation of mesoporous carbon with active nitrogen/oxygen configurations for sustainable triboelectric nanogenerator powered electro-Fenton degradation, Nano Energy 83 (2021) 105825. https://doi.org/10.1016/j.nanoen.2021.105825.

[34] Y. Zhu, M. Tian, Y. Chen, Y. Yang, X. Liu, S. Gao, 3D printed triboelectric nanogenerator self-powered electro-Fenton degradation of orange IV and crystal violet system using N-doped biomass carbon catalyst with tunable catalytic activity, Nano Energy 83 (2021) 105824. https://doi.org/10.1016/j.nanoen.2021.105824.

[35] B. Zhang, L. He, R. Zhang, W. Yuan, J. Wang, Y. Hu, Z. Zhao, L. Zhou, J. Wang, Z. L. Wang, Achieving material and energy dual circulations of spent lithium-ion batteries via triboelectric nanogenerator, Adv. Energy Mater. 13 (2023) 2301353. https://doi.org/10.1002/aenm.202301353.

[36] B. Zhang, L. He, J. Wang, Y. Liu, X. Xue, S. He, C. Zhang, Z. Zhao, L. Zhou, J. Wang, Z. L. Wang, Self-powered recycling of spent lithium iron phosphate batteries via triboelectric nanogenerator, Energy Environ. Sci. 16 (2023) 3873–3884. https://doi.org/10.1039/d3ee01156a.

[37] S. P. Ong, R. Tran, X-G. Li, J. H. Montoya, D. Winston, K. A. Perssonb, Anisotropic work function of elemental crystals, Surface Science 687 (2019) 48–55. https://doi.org/10.1016/j.susc.2019.05.002.

[38] W. Huang, Y. Huang, X. Huang, F. Shao, W. Liu, F. Kang, 3D leaf-like copper–zinc alloy enables dendrite-free zinc anode for ultra-long life aqueous zinc batteries, Small 20 (2024) 2404294. https://doi.org/10.1002/smll.202404294.

[39] A. Abdelhafiz, B. Wang, A. R. Harutyunyan, J. Li, Carbothermal shock synthesis of high entropy oxide catalysts: dynamic structural and chemical reconstruction boosting the catalytic activity and stability toward oxygen evolution reaction, Adv. Energy Mater. 12 (2022) 2200742. https://doi.org/10.1002/aenm.202200742.

[40] J. Song, C. Che, Y. Dai, J. Qin, C. Yang, Z. Chen, K. Ma, Y. Han, Y. Long, Inducing Cu charge redistribution by modulating proximity with $Zr(OH)_4$ for selective synthesis of imines and secondary amines with stoichiometric benzyl alcohol and nitrobenzene, ACS Catal. 15 (2025) 1170–1181. https://doi.org/10.1021/acscatal.4c05785.

[41] W. Gao, K. Xie, J. Xie, X. Wang, H. Zhang, S. Chen, H. Wang, Z. Li, C. Li, Alloying of Cu with Ru enabling the relay catalysis for reduction of nitrate to ammonia, Adv. Mater. 35 (2023) 2202952. https://doi.org/10.1002/adma.202202952.

[42] M. Zhang, Z. Ma, S. Zhou, C. Han, V. Kundi, P. V. Kumar, L. Thomsen, B. Johannessen, L. Peng, Y. Shan, C. Tsounis, Y. Yang, J. Pan, R. Amal, Surface engineering on Ag-decorated Co_3O_4 electrocatalysts for boosting nitrate reduction to ammonia, ACS Catal. 14 (2024) 11231–11242. https://doi.org/10.1021/acscatal.4c01510.

[43] S. Luo, H. Guo, T. Li, H. Wu, F. Zhang, C. Tang, G. Chen, G. Yang, Y. Zhou, Ruthenium-induced hydrolysis effect on Fe_2O_3 nanoarrays for high-performance electrochemical nitrate reduction to ammonia, Appl. Catal. B 351 (2024) 123967. https://doi.org/10.1016/j.apcatb.2024.123967.

[44] Y. Xu, Y. Wen, T. Ren, Z. Yu, H. Yu, K. Deng, Z. Wang, H. Wang, L. Wang, Synergistic multisite CuPdP nanodendrites for efficient ambient neutral electrosynthesis of ammonia from nitrate, Chem. Eng. J. 490 (2024) 151519. https://doi.org/10.1016/j.cej.2024.151519.

[45] K. Huang, K. Tang, M. Wang, Y. Wang, T. Jiang, M. Wu, Boosting nitrate to ammonia via the optimization of key intermediate processes by low-coordinated Cu–Cu Sites, Adv. Funct. Mater. 34 (2024) 2315324. https://doi.org/10.1002/adfm.202315324.

[46] X. Zhou, W. Xu, Y. Liang, H. Jiang, Z. Li, S. Wu, Z. Gao, Z. Cui, S. Zhu, Dynamically restructuring nanoporous Cu−Co electrocatalyst for efficient nitrate electroreduction to ammonia, ACS Catal. 14 (2024) 12251. https://doi.org/10.1021/acscatal.4c03336.

[47] X. Wang, Q. Hong, L. Shao, Q. Zhai, Y. Jiang, X. Ai, Y. Chen, S. Li, Copper–nickel oxide nanosheets with atomic thickness for high-efficiency sulfur ion electrooxidation assisted nitrate electroreduction to ammonia, Adv. Funct. Mater. 34 (2024) 2408834. https://doi.org/10.1002/adfm.202408834.

[48] A. Paliwal, C. D. Bandas, E. S. Thornburg, R. T. Haasch, A. A. Gewirth, Enhanced nitrate reduction activity from Cu-alloy electrodes in an alkaline electrolyte, ACS Catal. 13 (2023) 6754. https://doi.org/10.1021/acscatal.3c00999.

[49] Y. Zhao, Z. Bao, X. Bai, P. Xu, X. Shi, Q. Wu, Y. Jia, H. Zheng, L. Zheng, Superior electrocatalytic nitrate-to-ammonia conversion activity on CuCo bimetals in neutral media, Appl. Catal. B 357 (2024) 124294. https://doi.org/10.1016/j.apcatb.2024.124294.

[50] Q. Gou, Y. Mao, S. Lv, F. Gou, Y. Jiang, W. Shen, M. Li, Y. Wang, R. He, Enhancing nitrate reduction to ammonia by synergistic and interface coupling effects of binary metal sites, Appl. Catal. B 348 (2024) 123810. https://doi.org/10.1016/j.apcatb.2024.123810.

[51] M. A. Akram, B. Zhu, J. Cai, S. Qin, X. Hou, P. Jin, F. Wang, Y. He, X. Li, L. Feng, Hierarchical nanospheres with polycrystalline Ir&Cu and amorphous Cu_2O toward energy-efficient nitrate electrolysis to ammonia, Small 19 (2023) 2206966. https://doi.org/10.1002/smll.202206966.

[52] M. Xie, G. Zhu, H. Yang, B. Liu, M. Li, C. Qi, L. Wang, W. Jiang, P. Qiu, W. Luo, Periodic adjacent Pd-Fe pair sites for enhanced nitrate electroreduction to ammonia via accelerating proton relay, Adv. Energy Mater. 14 (2024) 2401717. https://doi.org/10.1002/aenm.202401717.

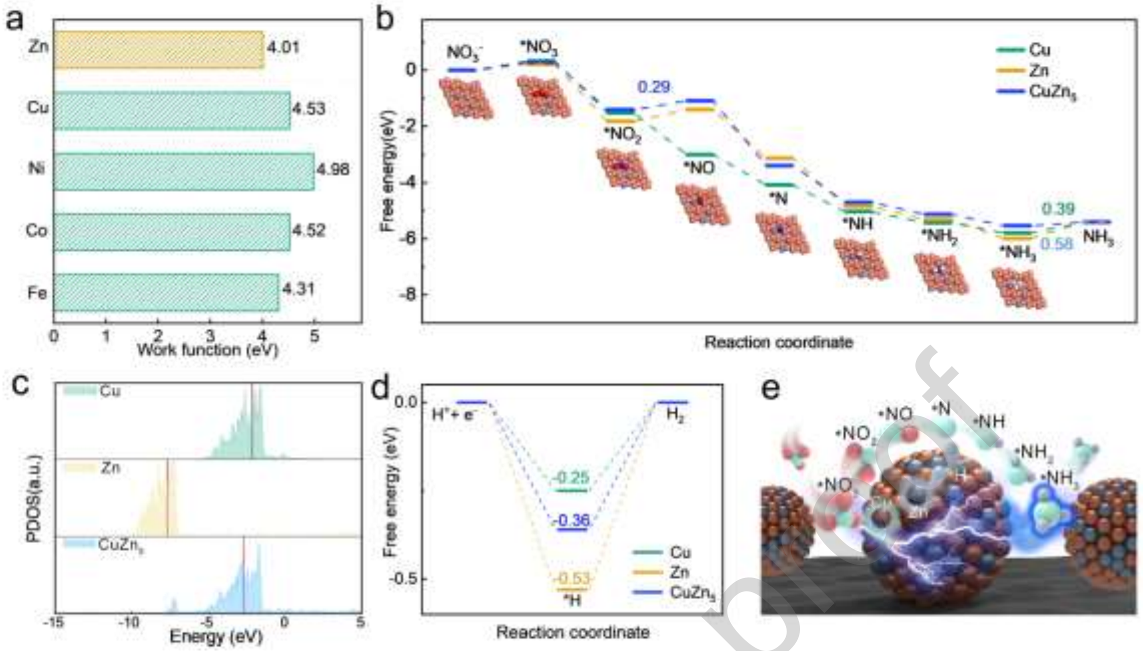

Figure 1. a) The work functions of Fe, Co, Ni, Cu and Zn. b) Gibbs free energies of varying intermediates are presented for different models. c) PDOS for the d-orbital and the associated d-band center positions. d) Gibbs free energy changes for H_2 formation. e) The proposed pathway of NO_3RR over $CuZn_5$.

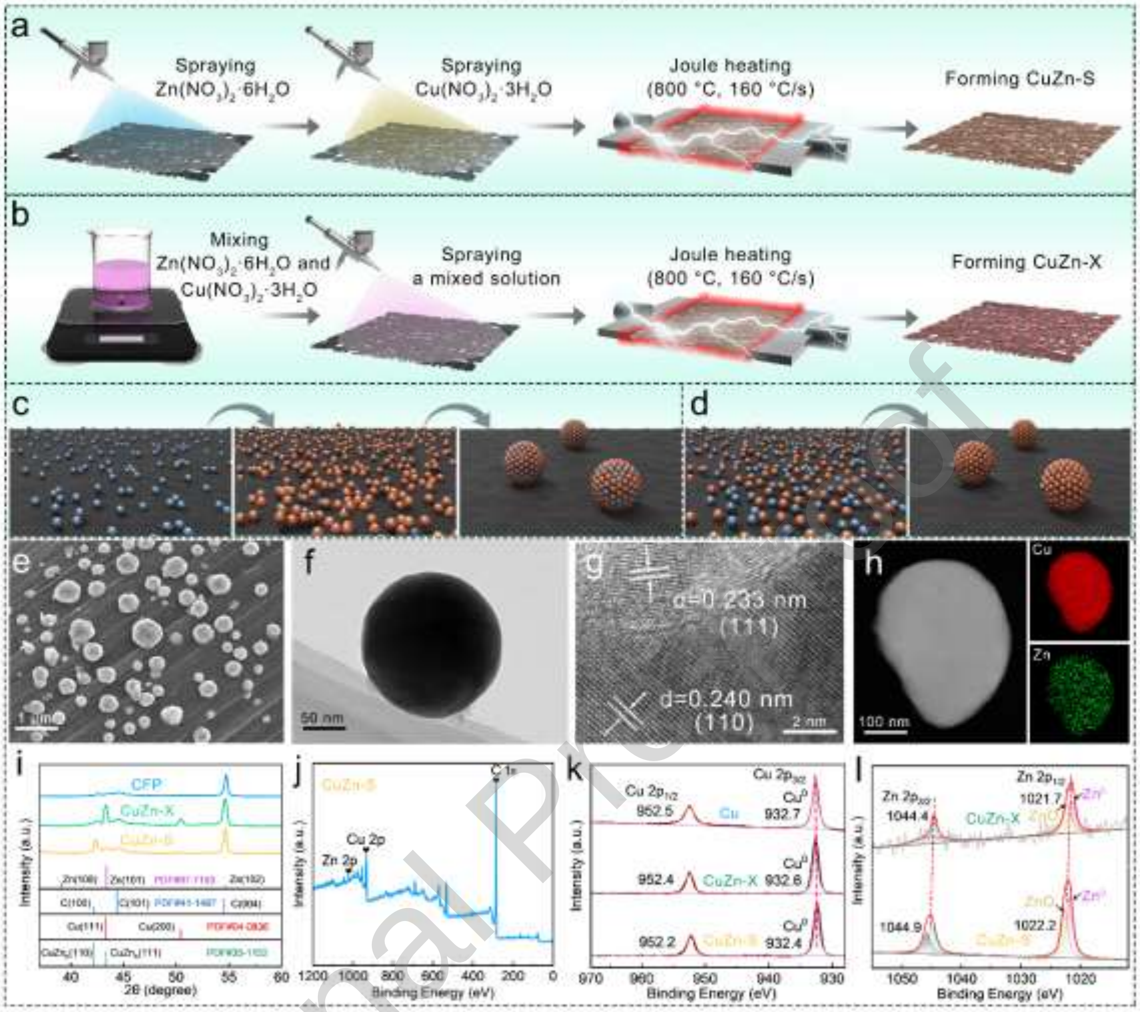

Figure 2. Characterizations of as-synthesized catalysts. Schematic illustrations for the synthesis method of a) CuZn-S catalysts and b) CuZn-X catalysts. c, d) Comparison of synthesis methods CuZn-S and CuZn-X. e) SEM image, f) TEM image, g) HRTEM and h) EDS of CuZn-S. i) XRD patterns of CFP, CuZn-X, and CuZn-S. j-l) Cu 2p and Zn 2p spectra of XPS of CuZn-S and CuZn-X.

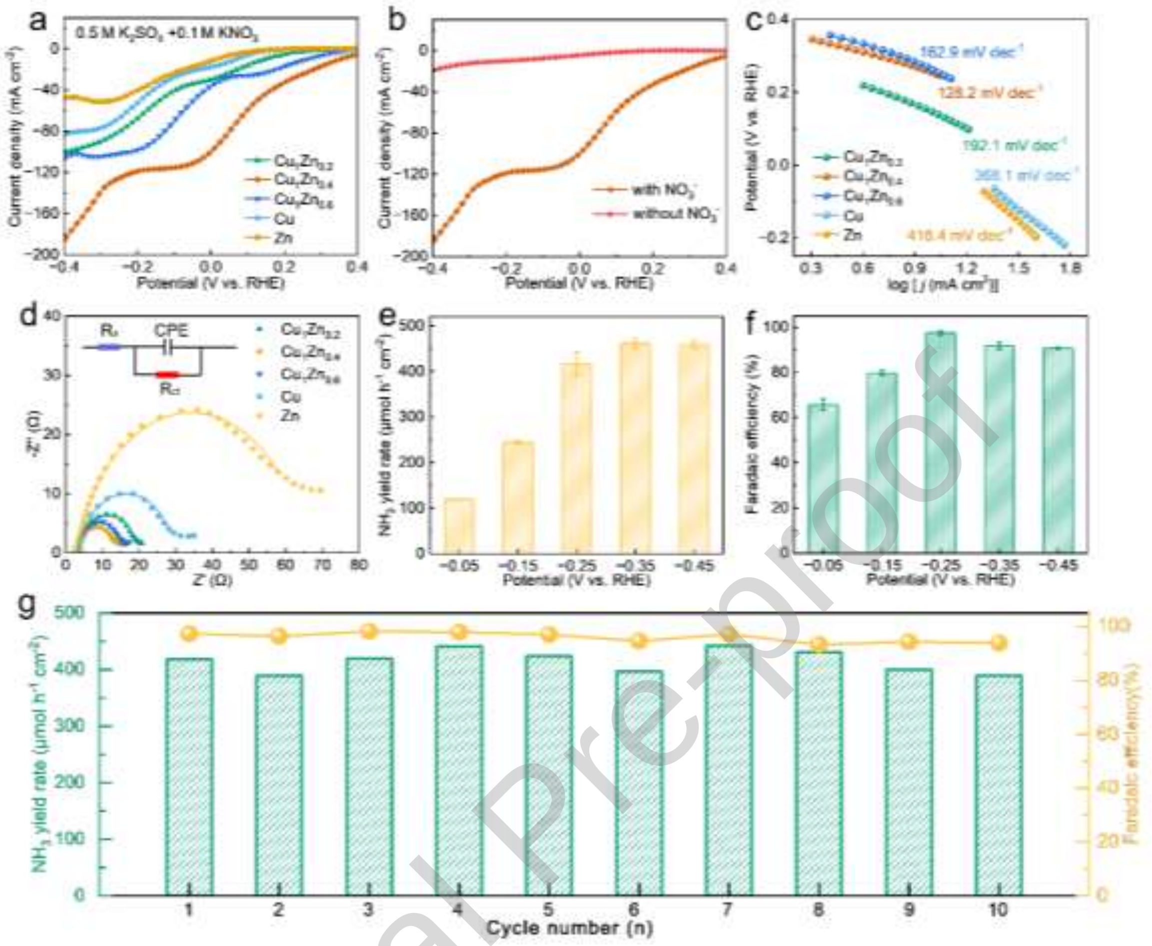

Figure 3. a) LSV curves of $Cu_1Zn_{0.2}$, $Cu_1Zn_{0.4}$, $Cu_1Zn_{0.6}$, Cu, and Zn tested in 0.5 M K_2SO_4 + 0.1 M KNO_3 solution. b) LSV curves of $Cu_1Zn_{0.4}$ tested in electrolyte with and without NO_3^-. c) Tafel slopes, d) EIS spectra of $Cu_1Zn_{0.2}$, $Cu_1Zn_{0.4}$, $Cu_1Zn_{0.6}$, Cu, and Zn. e) NH_3 yield rate, f) NH_3 FE of $Cu_1Zn_{0.4}$ at different potentials. g) Cycling tests of $Cu_1Zn_{0.4}$ for NO^- at −0.25 V vs. RHE.

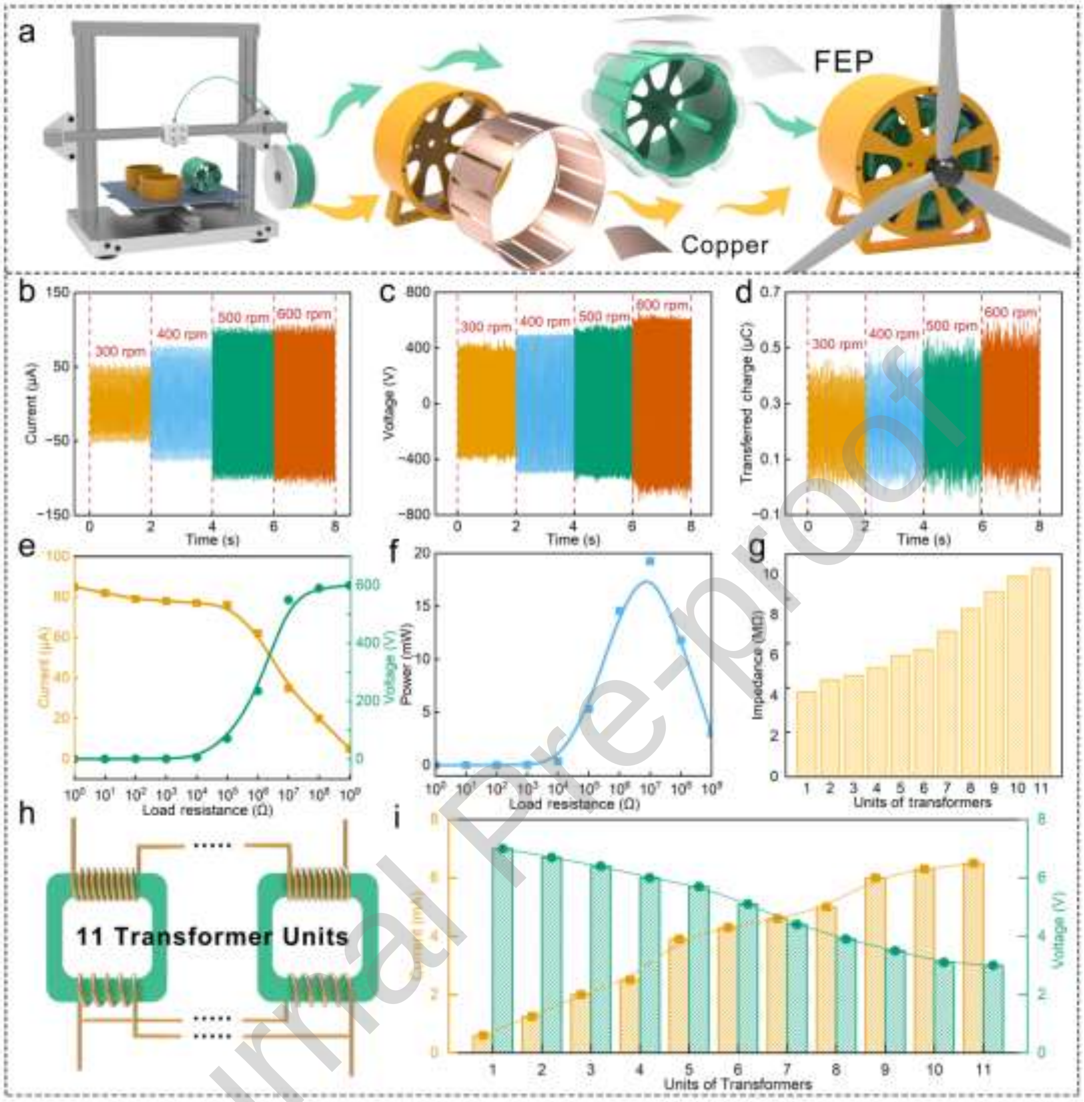

Figure 4. a) Schematic diagram of 3DP-TENG fabrication and assembly. Variation of b) short-circuit current, c) open-circuit voltage and d) transfer charge at different rotational speeds. e) The output current and voltage of the 3DP-TENG system are dependent on the resistance. f) Output peak-power-resistance profiles of 3DP-TENG system. g) The relationship between the resistance value and the number of transformers. h) the schematic representation of transformers connected in series. i) the rectified current and voltage outcomes subsequent to the serial concatenation of a diverse array of transformer units.

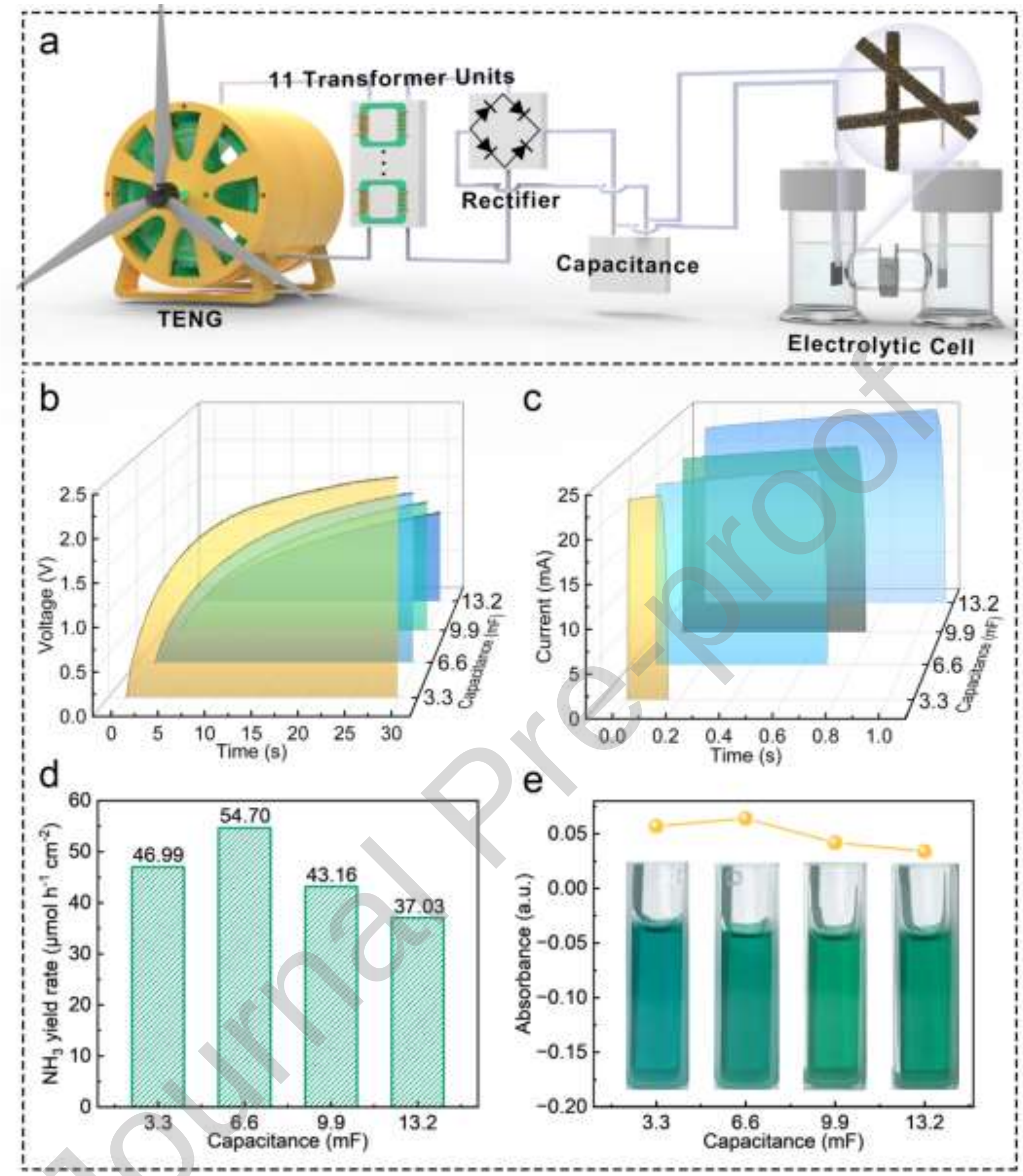

Figure 5. a) Schematic of the self-powered electrochemical NO_3RR system. b) the charging voltage of capacitors of different capacitances within 30 s. c) Discharge characteristics of a capacitor with a capacitance of different capacitances at a voltage of 2.8 V. d) Ammonia yield and e) absorbance when matching different capacitances.

CRediT authorship contribution statement

Shuaitong Wang: Conceptualization, Data Analysis, Writing – original draft. **Yang Liu:** Writing – review & editing. **Jinrui Huang:** Formal analysis, Software. **Shizhe Liu:** Visualization. **Shilong Li:** Formal analysis, Investigation. **Mengran Liu:** Validation, Investigation. **Zhichao Ma:** Investigation. **Tianfang Yang:** Writing – review & editing. **Yingjie Yang:** Data curation, Methodology. **Shuyan Gao:** Resources, Supervision, Writing – review & editing, Project administration, Funding acquisition. All authors discussed the results and commented on the manuscript.

Declaration of interests

☒ The authors declare that they have no known competing financial interests or personal relationships that could have appeared to influence the work reported in this paper.

☐The authors declare the following financial interests/personal relationships which may be considered as potential competing interests:

Shuaitong Wang, Yang Liu, Jinrui Huang, Shizhe Liu, Shilong Li, Mengran Liu, Zhichao Ma, Tianfang Yang, Yingjie Yang, Shuyan Gao

No conflict of interest exists for this work, which has been confirmed by all the authors.

Graphical abstract

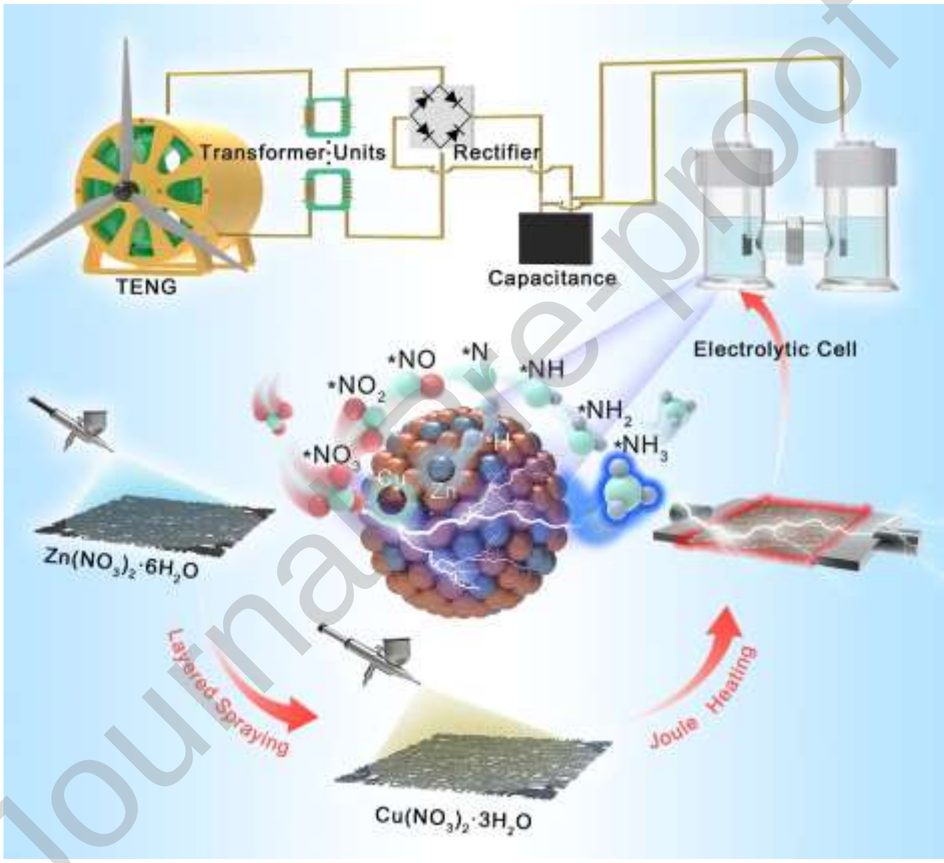

An innovative strategy involving layered spraying coupled with Joule heating is proposed for preparing $CuZn_5$ alloys. The synthesized $CuZn_5$ alloy enhances the adsorption energy of *H and reduces the desorption energy of NH_3. Furthermore, the $CuZn_5$ catalyst is integrated into a self-powered NO_3RR system, which is driven by a high-performance triboelectric nanogenerator without a power source.

Highlights

- Developing a highly efficient catalyst synthesis strategy of layered spraying coupled with Joule heating.
- Synthesizing the $CuZn_5$ alloy catalysts for enhancing the adsorption of *H.
- Constructing an innovative self-powered NO_3RR system by using TENG to replace traditional energy sources.